CHEMISTRY OF MATERIALS
Cite This: Chem. Mater. 2019, 31, 6880−6888
Article
pubs.acs.org/cm

Lead-Halide Perovskites Meet Donor−Acceptor Charge-Transfer Complexes

Nadège Marchal,*[,†] Wouter Van Gompel,[‡] María C. Gélvez-Rueda,[§] Koen Vandewal,[⊥] Kristof Van Hecke,[∥] Hans-Gerd Boyen,[⊥] Bert Conings,[⊥] Roald Herckens,[‡] Sudeep Maheshwari,[§] Laurence Lutsen,[#] Claudio Quarti,[†] Ferdinand C. Grozema,[§] Dirk Vanderzande,[‡] and David Beljonne[†]

[†]Laboratory for Chemistry of Novel Materials, University of Mons, Place du Parc, 20, B-7000 Mons, Belgium
[‡]Hybrid Materials Design (HyMaD), Institute for Materials Research (IMO-IMOMEC), Hasselt University, Martelarenlaan 42, B-3500 Hasselt, Belgium
[§]Optoelectronic Materials Section, Department of Chemical Engineering, Delft University of Technology, Van der Maasweg 9, 2629 HZ Delft, The Netherlands
[∥]XStruct, Department of Chemistry, Ghent University, Krijgslaan 281-S3, B-9000 Ghent, Belgium
[⊥]Institute for Materials Research, (IMO-IMOMEC), Hasselt University, Wetenschapspark 1, 3590 Diepenbeek, Belgium
[#]Associated Laboratory IMOMEC, IMEC, Wetenschapspark 1, B-3590 Diepenbeek, Belgium

Supporting Information

ABSTRACT: Low-dimensional lead halide hybrid perovskites are nowadays in the spotlight because of their improved stability and extensive chemical flexibility compared to their 3D perovskite counterparts, the current challenge being to design functionalized organic cations. Here, we report on the synthesis and full characterization of a perovskite-like hybrid (a perovskitoid) where the 1D lead iodide layout is patterned with a donor−acceptor charge transfer complex (CTC) between pyrene and tetracyanoquinodimethane, with a chemical formula of $(C_{20}H_{17}NH_3)PbI_3\cdot(C_{12}H_4N_4)$. By combining multiple structural analysis and spectroscopic techniques with ab initio modeling, we show that the electronic, optical, and charge-transport properties of the hybrid materials are dominated by the organic CTC, with the inorganic backbone primarily acting as a template for the organization of the donor and acceptor molecules. Interestingly, time-resolved microwave conductivity (TRMC) measurements show an enhanced photocurrent generation in the 1D hybrid compared to the pure organic charge-transfer salt, likely associated with transient localization of the holes on the lead-iodide octahedra. This observation is in line with the close energy resonance between the valence crystal orbitals of the lead-iodide lattice and the frontier occupied molecular orbitals of pyrene predicted by the DFT calculations. Therefore, it paves the way toward the design of new hybrid low-dimensionality perovskites offering a synergic combination of organic and inorganic functionalities.

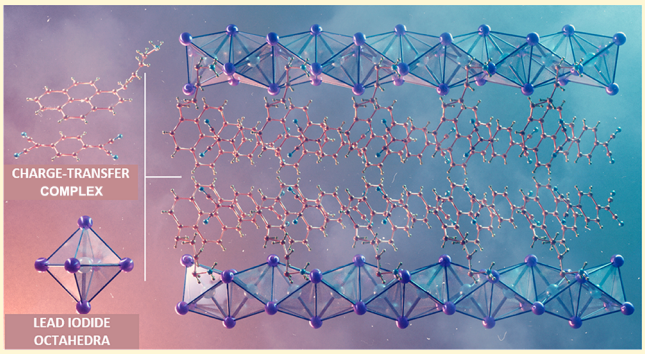

INTRODUCTION

Lead halide hybrid perovskites have received significant attention over the past decade as semiconductor materials, namely, for photovoltaic applications.[1−3] These materials possess a peculiar crystalline structure with an ABX_3 stoichiometry, where X is a halogen atom (I^-, Br^-, Cl^-), B an inorganic cation (Pb^{2+}, Sn^{2+}, ...), and A an organic cation ($CH_3NH_3^+$, $NH_2CHNH_2^+$). The structure consists of a three-dimensional network of corner-shared BX_6 octahedra with A cations located in the cavities of this framework.

While these 3D hybrid materials can be easily prepared from solutions of precursors and display impressive optoelectronic properties, e.g., with a certified power conversion efficiency of 24.2%,[4] they suffer from degradation issues mainly associated with ionic diffusion in the inorganic network.[5] This has driven the community to design low-dimensional hybrid perovskites that, in addition to higher stability, offer structural versatility, prompting their use as active components in a wide range of optoelectronic applications.[6−13] Indeed, the constraint that the organic cation should obey a strict geometrical rule to fit in the

Special Issue: Jean-Luc Bredas Festschrift

Received: April 1, 2019
Revised: August 1, 2019
Published: August 1, 2019

DOI: 10.1021/acs.chemmater.9b01289
Chem. Mater. 2019, 31, 6880−6888

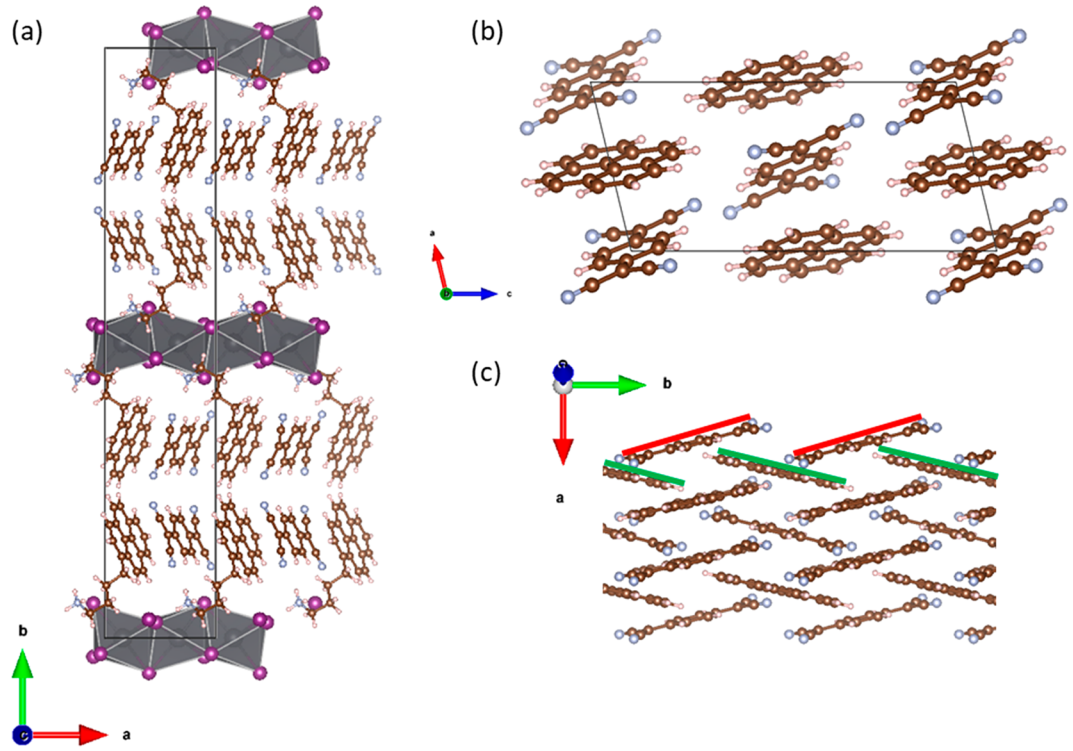

Figure 1. Crystal structures of the two investigated systems: (a) 1D hybrid $(PyrC_4NH_3)PbI_3{\cdot}(TCNQ)$; the box shows the unit cell. (b) Unit cell and (c) side view of the molecular arrangement of the organic CTC pyrene-TCNQ crystal, where TCNQ is highlighted by the red stick and pyrene by the green stick.[41] The atom labels represent hydrogen in white, nitrogen in blue-gray, carbon in brown, iodine in purple, and Pb in gray, inside the octahedra.

cavities created by the inorganic octahedral network in the 3D case is alleviated when going to lower-dimensionality materials.[14] As a result, by properly tuning the nature of the organic cation and/or the synthesis protocol, it is now possible to engineer lead halide organic−inorganic hybrids where the inorganic framework formed by the PbI_6^{4-} octahedra spans the full dimensionality range from 3D to 2D, 1D, or 0D.

Layered perovskite materials containing alkylammonium cations have been scrutinized in the past. While the study of these provides useful insight into the effects of dielectric confinement[15,16] and local lattice distortions,[17−20] the range of tunability offered by inert organic cations is limited. An attractive strategy to convey additional functionalities to the resulting hybrid materials is to replace the inert cations by electroactive organic conjugated molecules.[21−28]

Notable work in this direction includes the work of Evans et al.[29,30] and Maughan et al.,[31] who showed that synergic effects between the organic and inorganic components of hybrids can be achieved by making use of the process of charge transfer.

In the case of the TTF containing hybrids of Evans et al., charge transfer between a neutral organic molecule (TTF) and a radical cation ($TTF^{\bullet+}$) in the hybrid occurs. For the tropylium containing hybrid of Maughan et al., iodine-to-tropylium charge transfer was suggested.

Organic charge-transfer complexes (CTCs) have distinct optical fingerprints[32] and have been extensively studied over the last 50 years for their interesting properties, including ambipolar charge transport, metallicity, photoconductivity, and ferroelectricity.[32−37] In this context, we have recently shown that organic donor−acceptor charge-transfer complexes can be combined with 2D layered hybrid perovskites.[38] 2D perovskites with a nominal chemical formula $(PyrC_4NH_3)_2PbI_4{\cdot}2(TCNQ)$ or $(PyrC_4NH_3)_2PbI_4{\cdot}2(TCNB)$ with $PyrC_4$ being pyrene-C_4H_8 were obtained. The acceptors are incorporated into the organic layer through the formation of charge-transfer complexes with donors that are tethered to the inorganic framework via an alkylammonium chain. The acceptor molecule is therefore intercalated into the organic layer of the hybrid. In this regard, our work builds upon previous work on the intercalation of small molecules into the organic layer of 2D layered hybrids based on weak interactions, e.g., fluoroaryl−aryl interactions.[39,40] We note that our approach differs from the works of Evans et al. and Maughan et al., since we introduce separate organic donor and acceptor molecules that self-assemble into charge-transfer complexes in the organic layer of the hybrid. Introducing separate donor and acceptor molecules imparts a high potential tunability to our new type of hybrids.

Unfortunately, we were at that time not able to resolve single-crystal structures of these 2D hybrids, preventing detailed structure−property relationships to be unraveled. Here, we report on our ongoing efforts toward the synthesis of hybrid materials, in which the organic component contributes to the charge transport, combining in a synergic way the complementary properties of their organic and inorganic components. More specifically, we synthesized a novel 1D hybrid composed of wires of face-sharing PbI_6^{4-} octahedra separated by bilayers containing the CTCs, with a chemical formula of $(C_{20}H_{17}NH_3)PbI_3{\cdot}(C_{12}H_4N_4)$, which we rename as $(PyrC_4NH_3)PbI_3{\cdot}(TCNQ)$ (Figure 1a). A carbon chain of 4 carbon atoms ended by an ammonium group for the anchoring to the inorganic part is attached. This alkyl chain (which includes the positive charge of the cation via the ammonium

DOI: 10.1021/acs.chemmater.9b01289
Chem. Mater. 2019, 31, 6880−6888

group) is exclusively located on the pyrene molecule. The chains are running parallel to each other.

In addition to structural information, XPS valence band and TRMC measurements, combined with DFT computational investigations, provide detailed information about the electronic structure and the charge generation and transport properties of these novel hybrid materials. Altogether, our combined theory−experiment study conveys the message that (i) the inorganic lattice mostly acts as a template for the local organization of the organic conjugated molecules, and (ii) the close energy resonance between the occupied levels on the inorganic and organic parts improves photoinduced charge generation.

RESULTS AND DISCUSSION

Crystal Structure, Stability, and Film Morphology. The crystal structure of the mixed organic−inorganic hybrid has been elucidated using single-crystal X-ray diffraction (XRD) (Figure 1a) and was found to be monoclinic. The powder X-ray diffraction (PXRD) pattern of the bulk sample of crystals compared well with the simulated pattern from single-crystal XRD (Figure S1). The crystal structure of the pyrene-TCNQ organic CTC was taken from the literature, and a representation is shown in Figure 1b,c.[41] The experimental PXRD pattern of our grown pyrene-TCNQ crystals matched well with the simulated pattern based on the crystal structure from literature (Figure S2). The 1D hybrid perovskitoid shows very good thermal stability in ambient atmosphere. The compound does not degrade into a new phase until a temperature of ∼190 °C, as assessed based on temperature-controlled XRD measurements (Figures S13 and S14). Films for TRMC were prepared via drop-casting followed by thermal annealing. The morphology of the resulting films was investigated using SEM measurements (Figure S4). As can be seen, no clear pinholes are present in the film. The absence of significant pinholes is the most important criterion in terms of morphology for the analyses carried out in the current study. The morphology of the films could potentially be optimized by using different processing techniques (e.g., gas quenching or antisolvent dripping), but this is outside of the scope of the current study.

Electronic Structure and Optical Properties. Optical absorption spectra measured by photothermal deflection spectroscopy for the 1D hybrid perovskitoid and the organic CTC crystals are reported in Figure 2 (see also absorption spectra in Figures S5 and S6). While the shapes of the two spectra are similar, pointing to the similar nature of the involved electronic excited states, a clear shift of the sharp absorption onset from ∼1.3 eV for the organic CTC to ∼1 eV for the hybrid is observed. Such a spectral displacement might originate from various (combined) contributions, namely, a different molecular packing of the CTC or direct full or partial involvement of the lead halide inorganic skeleton through hybridization with the organic chromophores.

We resort to DFT electronic structure calculations to address the origin of the observed differences in electronic structure and optical properties between the organic and the hybrid crystals. As a first step, an in-depth study was performed to analyze the sensitivity of the results against details of the modeling methodology. It has indeed been widely documented that the inclusion of spin−orbit coupling (SOC) effects and an accurate treatment of electronic exchange and correlation energy are key to a quantitative description of the electronic

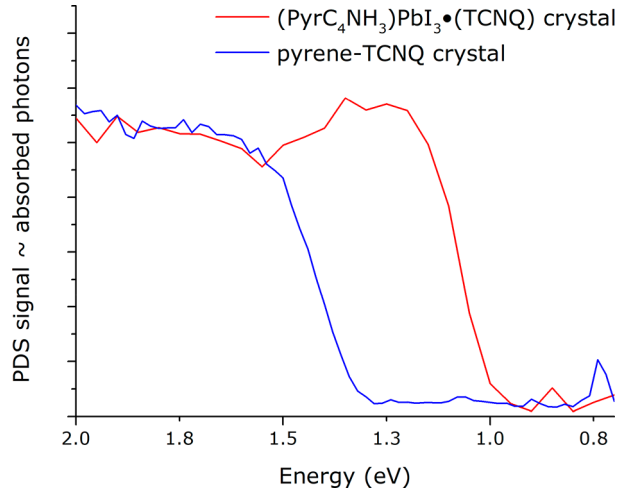

Figure 2. Optical absorption spectra of the 1D hybrid $(PyrC_4NH_3)PbI_3{\cdot}(TCNQ)$ and CTC pyrene-TCNQ single crystals measured using photothermal deflection spectroscopy (using a HeNe (633 nm) probe laser).

structure of lead halide perovskites.[42,43] Details about the modeling approach are provided in the Supporting Information (Table S1, Figure S7). In a nutshell, after realizing that SOC does not influence the lowest unoccupied energy levels (localized on the TCNQ acceptors), we selected (unless otherwise specified) plane-wave DFT calculations in combination with a hybrid functional (PBE0), as implemented in the Quantum Espresso package suite.[44] Using this methodology, we obtain an electronic bandgap of 1.93 eV for the 1D perovskitoid system, to be compared with 2.16 eV for the pure CTC crystal. While compared to the PDS data the theoretical values are expectedly blue-shifted, namely, by the exciton binding energy but also inherent errors associated with the choice of DFT functionals, the calculations do however correctly reproduce the observed spectral shift (∼0.23 eV calculated against ∼0.3 eV measured) between the two crystals.

Turning to the electronic structure energy diagrams displayed in Figure 3a, we find from the analysis of the partial density of states (DOS) that the band-edge levels in the 1D hybrid perovskitoid are fully confined on the organic part, namely, with the conduction band-edge (CBE) dominated by TCNQ empty orbitals and the valence band-edge (VBE) governed by pyrene occupied orbitals. It is important to stress, however, that the lead-iodide inorganic skeleton contributes with occupied crystalline orbitals that are located in close energy proximity (within ∼0.1 eV) to the VBE—in contrast, the corresponding PbI unoccupied crystalline orbitals are located at significantly higher energies than the CBE. In addition, inspection of the partial DOS reveals no or very limited hybridization between the organic molecular and inorganic crystalline orbitals, which would materialize through the presence of a partial contribution of lead and iodine atoms at the VBE (and CBE) energy. In view of the small energy difference, this absence of wave function mixing must originate from a very weak electronic coupling matrix element, likely resulting from the poor electronic contact between the inorganic scaffold and the conjugated chromophores. Looking retrospectively at the optical absorption data, we thus rule out hybridization as a mechanism for the observed red shift and rather invoke a reorganization of the donor and acceptor

DOI: 10.1021/acs.chemmater.9b01289
Chem. Mater. 2019, 31, 6880−6888

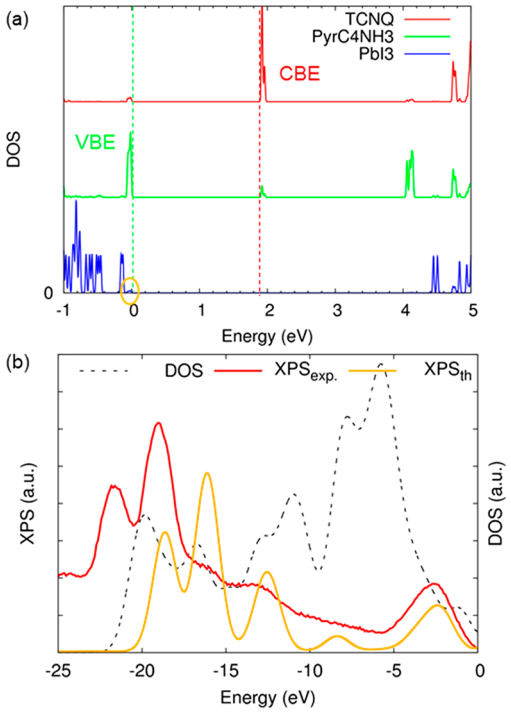

Figure 3. (a) Partial density of states for the different components of the 1D hybrid $(PyrC_4NH_3)PbI_3{\cdot}(TCNQ)$. The circled region indicates weak hybridization between the inorganic lattice and the CTC. VBE = valence band edge; CBE = conduction band edge; BG = band gap. (b) Comparison of the measured (by XPS in red) and calculated DOS of the 1D hybrid $(PyrC_4NH_3)PbI_3{\cdot}(TCNQ)$ (in dashed black). Contributions from different elements have been scaled according to their photoionization cross sections at the measured photon energy (1486.6 eV) to simulate the full theoretical XPS spectrum (in orange). It appears that lead (below −15 eV) and iodine (from −15 to 0 eV) related orbitals dominate completely the XPS signal.

molecules templated by the inorganic layout. This is consistent with the (slight) change in the ground-state charge transfer density when going from the organic CT salt (with an effective charge per TCNQ molecule calculated to be ∼0.15 |e| using a Bader charge analysis[45] reported in Supporting Information Table S2) to the lead halide CT hybrid (where the charge per TCNQ amounts to ∼0.21 |e|). We further note that the electronic band gap between the lead halide only crystalline orbitals is close to 4 eV at the level of theory considered. This is much higher than the corresponding bandgaps calculated at the same level of theory for 2D lead halide perovskites, highlighting the important role of dimensionality on the electronic structure of these materials.

Figure 3b displays both the predicted full (and partial) SOC-corrected DOS together with the simulated XPS spectrum, where relative intensities have been obtained through weighting the density of states by the relative photoionization cross sections of the involved valence electrons. While this approach should be considered with caution (as delocalized band states are obviously distinct from their contributing atomic orbitals), it explains the fact that occupied molecular orbitals arising from the organic components are hidden in the background noise of the XPS spectra because of their low ionization cross sections. With this caveat, we can proceed with the comparison of the theoretical results to the experimental valence band electronic structure, here probed using XPS (as a more bulk sensitive technique, information depth > 5 nm) instead of UPS (as a more surface sensitive technique, information depth about 1 nm). The measured and predicted valence band spectra are dominated by the iodine atoms at low binding energies, while the SOC-split 5d orbitals of lead contribute a twin peak at higher binding energies (below −10 eV). It is interesting to see that a better match with experiment regarding the absolute energies of the lead orbitals is obtained considering the bare (unscaled) DOS, which could indicate partial hybridization or simply reflect uncertainties in the computed orbital energies. Unfortunately, the limited spectral resolution and the low cross sections of the sp2 carbon atoms from the pyrene molecules do not allow the theoretical finding that the VBE is mostly sourced by the organic molecules to be ascertained. As demonstrated below, this is indirectly supported by charge transport measurements.

Charge Transport Properties. Table 1 reports the calculated effective masses along high-symmetry paths for (i) the hybrid 1D organic−inorganic perovskitoid; (ii) the pure organic CT salt; and (iii) a hypothetical system built by removing all lead and iodine atoms from the crystal structure of the hybrid material and (to balance the charges) substituting the nitrogen atoms of the ammonium groups with carbons. This aims at mimicking a pure template effect where the inorganic lattice would participate not directly to the transport properties but eventually indirectly through a reorganization of the spatial rearrangement of the donor and acceptor molecules in comparison to the CT salt. As a matter of fact, in all relevant directions, the effective masses predicted by the DFT calculations are typical for organic molecular crystals with weak band dispersion. The differences observed between the hybrid and the organic crystal primarily stem from a template effect, as confirmed by comparing the relatively similar effective masses computed for the real hybrid and hypothetical structures. This template effect materializes mostly as differences in intermolecular distances along TCNQ and pyrene molecular rows in the *b* direction for the CTC crystal and the corresponding *c* direction for the 1D hybrid perovskitoids; see Figure 1c. More specifically, there is a reduced herringbone angle, or similarly a smaller longitudinal molecular translation, between successive donor (acceptor) molecules in the hybrid structure. While this is still far from being ideal from an intermolecular spatial overlap perspective, there is improved $\pi-\pi$ stacking interaction between the organic molecules in the perovskitoid 1D systems compared to the pure CTC crystal,

Table 1. Effective Masses of Electrons and Holes for the CTC Crystal and the 1D Hybrid $(PyrC_4NH_3)PbI_3{\cdot}(TCNQ)$ Crystals[a]

	organic CTC pyrene-TCNQ		1D CTC pyrene-TCNQ		1D hybrid $(PyrC_4NH_3)PbI_3{\cdot}(TCNQ)$	
direction	m_{e-}	m_{h+}	m_{e-}	m_{h+}	m_{e-}	m_{h+}
(100)	10.42	3.29	4.31	∞	4.63	∞
(010)	**9.90**	**2.11**	∞	∞	∞	∞
(001)	6.66	13.85	7.37	2.35	**4.33**	**1.62**

[a]We have also considered a hypothetical system (1D CTC) obtained by removing the inorganic layout from 1D hybrid perovskitoids structure in order to highlight the template effect. Values in bold emphasize the reduced effective masses when going from the CTC to the 1D hybrid material.

DOI: 10.1021/acs.chemmater.9b01289
Chem. Mater. 2019, 31, 6880−6888

which is driven by the inorganic layout. As a result, the electron effective masses along the high-mobility direction (c) are significantly smaller, especially for electrons, in the hybrid material with respect to the pure salt (for which b is the high-mobility direction), a difference that reflects the more substantial wave function overlap between the molecular orbitals in the presence of the inorganic template. Yet, the absolute values of the effective masses remain relatively large for both holes and electrons, irrespective of the direction; hence, we expect relatively poor charge transport mobility for both organic and hybrid crystals.

This is fully confirmed by time-resolved micro-conductivity (TRMC) measurements that probe the change in conductivity due to mobile charge carriers using high-frequency microwaves. The charge carriers can be generated either by a high energy electron pulse (pulse-radiolysis TRMC) or by a laser (photoconductivity TRMC). We have performed PR-TRMC measurements to monitor the temperature-dependent mobility of free charge carriers in the two materials. The formation of free charge carriers is assured by the effective irradiation energy (~20 eV) from the electron pulse.[46,47] The results plotted in Figure 4a show modest (10^{-3}–10^{-2} cm^2 V^{-1} s^{-1}) and similar

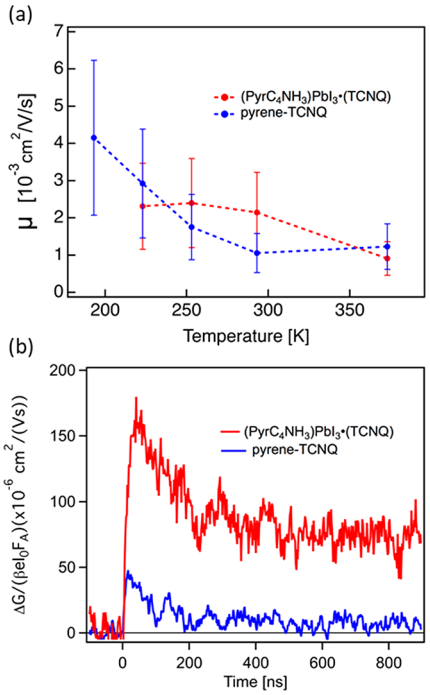

Figure 4. (a) Charge carrier mobility as a function of temperature for the two investigated systems: 1D hybrid $(PyrC_4NH_3)PbI_3{\cdot}(TCNQ)$ and the CTC crystal pyrene-TCNQ. (b) Photoconductivity TRMC measurements of 1D hybrid $(PyrC_4NH_3)PbI_3{\cdot}(TCNQ)$ and the CTC crystal pyrene-TCNQ excited at the CT states (~600 nm).

mobility values over a broad temperature range in the pure organic salt and in the 1D organic–inorganic hybrid crystals. In addition, similar recombination dynamics of the charge carriers for both materials are obtained; see Supporting Information (Figure S9 and S10).

To complement these studies, photoconductivity TRMC measurements have also been performed with laser excitation at different wavelengths (excitonic peak at ~500 nm and charge-transfer state at ~600 nm). In these measurements, the photoconductivity signal obtained is the product of the mobility and the yield of photogenerated free electrons and holes.[47,48] Exciting in the charge-transfer band results in a larger photoconductivity signal for the 1D hybrid perovskitoid compared to the organic salt; see Figure 4b. Besides, the recombination lifetime of the charge carriers is longer. As mentioned above, no appreciable difference in charge carrier mobility could be measured from the PR-TRMC experiments. Therefore, we conclude that the higher photoconductivity signal in the hybrid film must be caused by a higher yield of mobile free charge carriers in the 1D organic–inorganic hybrid crystals (a more detailed description of the PR-TRMC and photoconductivity TRMC results can be found in the Supporting Information). We speculate that the larger fraction of photogenerated free charge carriers in the hybrid material is related to transient localization of the holes on the inorganic lattice facilitated by the close energy spacing between the occupied inorganic crystalline and organic molecular occupied orbitals, *vide supra*.

CONCLUSIONS

We have reported on the synthesis of a novel, thermally stable, 1D hybrid material where charge-transfer complexes between molecular donors and acceptors act as charge compensating organic cations, thus offering new functionalities to the resulting hybrid materials. These have been extensively characterized using a battery of structural analysis and spectroscopic techniques in combination with molecular modeling. Our investigations show that most of the electronic and optical properties of the CTC salt are retained, with the inorganic lattice primarily acting as a template for the spatial arrangement of the molecular chromophores. As a result, modest charge transport properties with charge carrier mobility not exceeding 10^{-2} $cm^2V^{-1}s^{-1}$ have been obtained. However, a first indication pointing toward some coupling between the inorganic and organic manifolds in these mixed systems is the increased photocurrent generation, likely favored by transient localization of the holes on the lead halide backbone. Moreover, the novel hybrids discussed in this article offer a high degree of potential tunability. As can be deduced from the general formula $(D\text{-}C_nH_{2n}\text{-}NH_3)PbX_3{\cdot}(A)$, one could potentially change the core of the donor molecule (D), the alkyl chain length of the donor molecule (C_nH_{2n}), the acceptor molecule (A) and the halide (X). All of these changes are suspected to have a (more or less significant) degree of influence on the optical and electronic properties of these hybrids. Therefore, the applicability of this type of hybrids can potentially be extended by using donor:acceptor combinations with superior charge transport properties compared to pyrene-TCNQ. Charge-transfer complexes can also exhibit a variety of electronic or magnetic properties and it would be interesting to determine how their inclusion into an inorganic scaffold influences these.

EXPERIMENTAL METHODS

Chemicals and Reagents. 7,7,8,8-Tetracyanoquinodimethane (TCNQ, >98.0%) was bought from TCI. Potassium phthalimide salt (95%) was obtained from Fluorochem. Lead iodide (PbI_2, 99.999%) was obtained from Lumtec. 1-Pyrenebutyric acid (95%) was purchased from Combi-Blocks, Inc. Lithium aluminum hydride ($LiAlH_4$, 95%), carbon tetrabromide (CBr_4, 98%), potassium carbonate (K_2CO_3, 99+%), magnesium sulfate ($MgSO_4$, 99%), ammonium chloride (NH_4Cl, 99+%), triphenylphosphine (Ph_3P, 99%), pyrene (98%), hydrazine monohydrate (65%), and hydriodic

DOI: 10.1021/acs.chemmater.9b01289
Chem. Mater. 2019, 31, 6880–6888

acid (57 wt % aqueous solution) were bought from Fisher Scientific. All chemicals were used without further purification. The dry dimethylformamide (DMF) that was used to make the precursor solutions and dry tetrahydrofuran (THF), which was used for the reactions, were obtained from our in-house solvent-purification system (MBRAUN SPS-800). All other solvents were purchased from Fisher Scientific.

The $PyrC_4NH_3I$ salt was synthesized as detailed in a previous publication.[10]

Single Crystal Growth. The single crystals of $(PyrC_4NH_3)PbI_3\cdot(TCNQ)$ were grown using an antisolvent vapor-assisted crystallization approach[49] in which the components are dissolved together in a good solvent (gamma-butyrolactone; GBL) and dichloromethane (DCM) antisolvent slowly diffuses into the GBL solution. Specifically, $PyrC_4NH_3I$ (0.108 mol/L), TCNQ (0.108 mol/L), and PbI_2 (0.108 mol/L) were dissolved together in gamma-butyrolactone by stirring at 50 °C for 15 min. The precursor solution was filtered through a syringe filter (0.45 μm). The precursor solution (0.5 mL) was transferred to a small glass vial. The small vial (5 mL volume) was capped off with aluminum foil. A small hole was made in the aluminum foil. The small vial with the aluminum foil was put in a larger glass vial (20 mL volume). A small amount of dichloromethane (2 mL) was injected in the gap between the two flasks, and the larger flask was capped off with a plastic cap and parafilm. The vials were left undisturbed at room temperature. After 1 week black crystals suitable for single-crystal X-ray diffraction were harvested. These crystals were washed three times with dry dichloromethane and were subsequently dried under reduced pressure at room temperature.

The crystals of the organic CTC pyrene-TCNQ were grown by dissolving equimolar amounts of pyrene (0.025 mol/L) and TCNQ (0.025 mol/L) in tetrahydrofuran (THF) by stirring at 40 °C until full dissolution. The solution was allowed to cool down to room temperature and was filtered through a syringe filter (0.45 μm). Crystals were obtained by evaporation of the THF at room temperature.

Thin Film Deposition. Stoichiometric amounts of $PyrC_4NH_3I$ (0.3 mol/L), TCNQ (0.3 mol/L), and PbI_2 (0.3 mol/L) were dissolved in dry DMF by stirring at 50 °C for 30 min. The precursor solution was filtered through a syringe filter (0.45 μm) before use.

Quartz substrates were cleaned through consecutive sonication steps in a series of solvents (detergent water, deionized water, acetone, isopropanol) for 15 min each, followed by a UV-ozone treatment for 15 min. Films were obtained by drop-casting (~30 μL on a 2.5 cm × 2.5 cm substrate) on a quartz substrate. The films were annealed at 110 °C for 15 min.

Characterization. *X-ray Diffraction.* X-ray diffraction measurements were performed at room temperature in ambient air on a Bruker D8 Discover diffractometer with Cu Kα radiation. Temperature-controlled XRD measurements were performed on the same instrument with a temperature cell, under nitrogen flow.

Photothermal Deflection Spectroscopy Measurements. Photothermal deflection spectroscopy (PDS) was performed using a home-built setup: chopped (4.1 Hz) monochromatic light from a 100 W Quartz-Tungsten-Halogen lamp is focused onto the crystal. The crystal is glued onto a quartz substrate with inert transparent glue (ethyl-2-cyanoacrylate). Substrate and sample are immersed in perfluorohexane (C_6F_{14}, 3 M Fluorinert FC-72). A HeNe (633 nm) probe laser passes through the deflection medium and grazes the surface of the sample. Absorption of monochromatic light results in a slight heating of sample and deflection medium. The latter has a strongly temperature dependent refractive index, resulting in deflection of the probe laser, of which the amplitude is detected by a position-sensitive Si detector, connected to a Stanford Research Systems SR830 lock-in amplifier. The incident light intensity is measured at the same time by a pyro-electric detector. The PDS signal is obtained by dividing the deflection signal by the signal coming from the pyroelectric detector and is for weakly emissive samples proportional to the absorption spectrum.[50]

Valence Band Spectroscopy. Valence band spectroscopy was carried out on a commercial electron spectrometer (PHI-5600LS), equipped with a smallspot X-ray source providing monochromatized Al K radiation (photon energy 1486.6 eV). During the XPS measurements, an overall energy resolution (photons and electrons) of 0.36 eV full width at half-maximum (fwhm) was applied.

Pulse-Radiolysis Microwave Conductivity Measurements. High energy pulse microwave conductivity measurements were performed on micrometer crystals (~ 45 mg) placed in a polyether ether ketone (PEEK) holder. The PEEK block with the sample is placed inside a rectangular waveguide cell (chemically inert gold-plated copper). The cell is contained in a cryostat in which the temperature can be varied between 123 and 473 K. The irradiation intensity was varied between pulse lengths of 5 and 50 ns (charge carrier concentrations ~2×10^{16} cm^{-3} to 2×10^{17} cm^{-3}) for each temperature at a frequency of 31 GHz. The frequency scan (28−38 GHz) fits were measured at a pulse length of 20 ns (~9.9×10^{16} cm^{-3}).

Photoconductivity Measurements. Laser induced time-resolved microwave conductivity (TRMC) measurements were performed on thin films deposited on quartz substrates and placed in a sealed resonant cavity inside a nitrogen-filled glovebox. Photoconductivity TRMC measurements quantify the change in conductivity [microwave (8−9 GHz) power] upon pulsed excitation (repetition rate 10 Hz) due to free mobile charge carriers. The change of microwave power is related to the change in conductivity before and during the photoconductance measurements, and the samples were kept in an inert nitrogen environment to prevent degradation by exposure to moisture.

THEORETICAL METHODS

Electronic Properties. Density functional theory calculations[51−55] with periodic boundary conditions have been performed with the Quantum Espresso suite program[44] for the electronic properties (and Bader analysis[45]) using a planewave/pseudopotential formalism. We adopted a norm-conserving pseudopotential, with a cutoff of 40 Ry for the expansion of the wave function and a correction for the van der Waals interactions (Grimme DFT-D2 method[56]). Different functionals (GGA and Hybrids) were applied: PBE,[57] PBE0, and HSE. In the case of the PBE functional, we also performed the same calculations with and without a spin−orbit correction. We kept the same k-points mesh for all PBE calculations, 4 × 3 × 2 for the organic crystal (pyrene-TCNQ) and 4 × 1 × 4 for the 1D perovskitoid. When using hybrid functionals, the calculations were limited at the gamma point of the first Brillouin zone, because of the calculation costs.

Charge Transport Properties. Effective mass calculations have also been performed with Quantum Espresso at the PBE level. We instead resorted to the CRYSTAL suite program (CRYSTAL14,[58,59] CRYSTAL17[60,61]) for effective mass calculations using hybrid functionals, namely, the PBE0 functional, as these are not implemented in Quantum Espresso. For consistency between the two sets of results, we paid attention to keep the same cell parameters, the same number of atoms explicitly taken into account and the same k-points mesh for the single point calculations.

ASSOCIATED CONTENT

Supporting Information

The Supporting Information is available free of charge on the ACS Publications website at DOI: 10.1021/acs.chemmater.9b01289.

Crystallographic information file (CIF)

Experimental details of the single crystal XRD measurement, powder XRD, comparison between 2D and 1D hybrids containing CTCs, scanning electron microscopy, absorption spectra, theoretical methodological study, Bader analysis, partial density of states, pulse-radiolysis TRMC, photoconductivity TRMC, and thermal stability of the hybrid (PDF)

DOI: 10.1021/acs.chemmater.9b01289
Chem. Mater. 2019, 31, 6880−6888

AUTHOR INFORMATION

Corresponding Author

*(N.M.) E-mail: nadege.marchal@umons.ac.be.

ORCID

Wouter Van Gompel: 0000-0002-8173-5206
Koen Vandewal: 0000-0001-5471-383X
Kristof Van Hecke: 0000-0002-2455-8856
Hans-Gerd Boyen: 0000-0003-0711-7597
Bert Conings: 0000-0002-3830-1971
Claudio Quarti: 0000-0002-5488-1216
Ferdinand C. Grozema: 0000-0002-4375-799X
Dirk Vanderzande: 0000-0002-9110-124X
David Beljonne: 0000-0002-2989-3557

Author Contributions

The manuscript was written through contributions of all authors. All authors have given approval to the final version of the manuscript.

Notes

The authors declare no competing financial interest.

ACKNOWLEDGMENTS

The FWO is acknowledged for the funding of research. W.V.G. is an SB Ph.D. fellow at FWO (Number 1S17516N), R.H. is a special research fund (BOF) doctoral (Ph.D.) student at UHasselt/IMO. K.V.H. thanks the Hercules Foundation (Project AUGE/11/029 "3D-SPACE: 3D Structural Platform Aiming for Chemical Excellence") and the special research fund (BOF) − Ugent (Project 01N03217) for funding. The work has been carried out in the context of the solliance network (www.solliance.eu), of which UHasselt and TUDelft are members. Additionally UHasselt is a partner in the Energyville Consortium (http://www.energyville.be/about-energyville). The research leading to these results in the Delft University of Technology has received funding from the European Research Council Horizon 2020 ERC Grant Agreement No. 648433. The work from the University of Mons was supported by a 50-50 Ph.D. funding for N.M. from the University of Mons, by the Interuniversity Attraction Pole program of the Belgian Referal Science Policy Office (PAI 6/27) and FNRS-F.R.S. Computational resources have been provided by the Consortium des Equipements de Calcul Intensif (CECI), funded by the Fonds de la Recherche Scientifique de Belgique (F.R.S.-FNRS) under Grant No. 2.5020.1 and by the Walloon Region. C.Q. and D.B. are a FNRS postdoctoral researcher and research director, respectively. Bart Ruttens and Jan D'Haen (IMO-IMOMEC) are acknowledged for PXRD measurements.

REFERENCES

(1) Shi, Z.; Jayatissa, A. Perovskites-Based Solar Cells: A Review of Recent Progress, Materials and Processing Methods. *Materials* **2018**, *11* (5), 729.

(2) Kojima, A.; Teshima, K.; Shirai, Y.; Miyasaka, T. Organometal Halide Perovskites as Visible-Light Sensitizers for Photovoltaic Cells. *J. Am. Chem. Soc.* **2009**, *131*, 6050−6051.

(3) Stranks, S. D.; Snaith, H. J. Metal-halide perovskites for photovoltaic and light-emitting device. *Nat. Nanotechnol.* **2015**, *10* (5), 391−402.

(4) https://www.nrel.gov/pv/assets/pdfs/best-research-cell-efficiencies-190416.pdf (accessed July 31, 2019).

(5) Meng, L.; You, J.; Yang, Y. Addressing the stability issue of perovskite solar cells for commercial applications. *Nat. Commun.* **2018**, *9*, 5265.

(6) Grancini, G.; Roldàn-Carmona, C.; Zimmermann, I.; Mosconi, E.; Lee, X.; Martineau, D.; Narbey, S.; Oswald, F.; De Angelis, F.; Gratzel, M.; et al. One Year Stable Perovskite Solar Cells by 2D/3D Interface Engineering. *Nat. Commun.* **2017**, *8*, 15684.

(7) Saidaminov, M. I.; Mohammed, O. F.; Bakr, O. M. Low-Dimensional-Networked Metal Halide Perovskites: The Next Big Thing. *ACS Energy Lett.* **2017**, *2* (4), 889−896.

(8) Lin, H.; Zhou, C.; Tian, Y.; Siegrist, T.; Ma, B. Low-Dimensional Organometal Halide Perovskites. *ACS Energy Lett.* **2018**, *3* (1), 54−62.

(9) Etgar, L. The Merit of Perovskite's Dimensionality; Can. This Replace the 3D Halide Perovskite? *Energy Environ. Sci.* **2018**, *11* (2), 234−242.

(10) Van Gompel, W. T. M.; Herckens, R.; Van Hecke, K.; Ruttens, B.; D'Haen, J.; Lutsen, L.; Vanderzande, D. Low-dimensional Hybrid Perovskites Containing an Organic Cation with an Extended Conjugated System: Tuning the Excitonic Absorption Features. *Chem. Nano Mat* **2019**, *5* (3), 323−327.

(11) Mao, L.; Stoumpos, C. C.; Kanatzidis, M. G. Two-Dimensional Hybrid Halide Perovskites: Principles and Promises. *J. Am. Chem. Soc.* **2019**, *141* (3), 1171−1190.

(12) Grancini, G.; Nazeeruddin, M. K. Dimensional Tailoring of Hybrid Perovskites for Photovoltaics. *Nat. Rev. Mater.* **2019**, *4* (1), 4−22.

(13) Herckens, R.; Van Gompel, W. T. M.; Song, W. Y.; Gelvez-Rueda, M. C.; Maufort, A.; Ruttens, B.; D'Haen, J.; Grozema, F. C.; Aernouts, T.; Lutsen, L.; Vanderzande, D. Multi- layered hybrid perovskites templated with carbazole derivatives: optical properties, enhanced moisture stability and solar cell characteristics. *J. Mater. Chem. A* **2018**, *6* (45), 22899−22908.

(14) Amat, A.; Mosconi, E.; Ronca, E.; Quarti, C.; Umari, P.; Nazeeruddin, M. K.; Graetzel, M.; De Angelis, F. Cation-Induced Band Gap Tuning in Organohalide Perovskites: Interplay of Spin-Orbit Coupling and Octahedral Tilting. *Nano Lett.* **2014**, *14*, 3608−3616.

(15) Even, J.; Pedesseau, L.; Katan, C. Understanding Quantum Confinement of Charge Carriers in Layered 2D Hybrid Perovskites. *ChemPhysChem* **2014**, *15*, 3733−3741.

(16) Sapori, D.; Kepenekian, M.; Pedesseau, L.; Katan, C.; Even, J. Quantum Confinement and Dielectric Profiles of Colloidal Nanoplatelets of Halide Inorganic and Hybrid Organic-Inorganic Perovskites. *Nanoscale* **2016**, *8*, 6369−6378.

(17) Quarti, C.; Marchal, N.; Beljonne, D. Tuning the Optoelectronic Properties of Two-Dimensional Hybrid Perovskite Semiconductors with Alkyl Chain Spacers. *J. Phys. Chem. Lett.* **2018**, *9* (12), 3416−3424.

(18) Gan, L.; Li, J.; Fang, Z.; He, H.; Ye, Z. Effects of Organic Cation Length on Exciton Recombination in Two-Dimensional Layered Lead Iodide Hybrid Perovskite Crystals. *J. Phys. Chem. Lett.* **2017**, *8*, 5177−5183.

(19) Traore, B.; Pedesseau, L.; Assam, L.; Che, X.; Blancon, J.-C.; Tsai, H.; Nie, W.; Stoumpos, C. C.; Kanatzidis, M. G.; Tretiak, S.; et al. Composite Nature of Layered Hybrid Perovskites: Assessment on Quantum and Dielectric Confinements and Band Alignment. *ACS Nano* **2018**, *12*, 3321−3332.

(20) Motta, C.; El-Mellouhi, F.; Kais, S.; Tabet, N.; Alharbi, F.; Sanvito, S. Revealing Hte Role of Organic Cations in Hybrid Halide Perovskite CH3NH3PbI3. *Nat. Commun.* **2015**, *6*, 7026.

(21) Mitzi, D. B.; Chondroudis, K.; Kagan, C. R. Design, Structure, and Optical Properties of Organic-Inorganic Perovskites Containing an Oligothiophene Chromophore. *Inorg. Chem.* **1999**, *38* (26), 6246−6256.

(22) Chondroudis, K.; Mitzi, D. B. Electroluminescence from an Organic-Inorganic Perovskite Incorporating a Quaterthiophene Dye within Lead Halide Perovskite Layers. *Chem. Mater.* **1999**, *11* (11), 3028−3030.

DOI: 10.1021/acs.chemmater.9b01289
Chem. Mater. 2019, 31, 6880−6888

(23) Cortecchia, D.; Soci, C.; Cametti, M.; Petrozza, A.; Martí-Rujas, J. Crystal Engineering of a Two-Dimensional Lead-Free Perovskite with Functional Organic Cations by Second-Sphere Coordination. *ChemPlusChem* **2017**, *82*, 681−685.
(24) Jemli, K.; Audebert, P.; Galmiche, L.; Trippé-Allard, G.; Garrot, D.; Lauret, J. S.; Deleporte, E. Two-Dimensional Perovskite Activation with an Organic Luminophore. *ACS Appl. Mater. Interfaces* **2015**, *7*, 21763−21769.
(25) Savory, C. N.; Palgrave, R. G.; Bronstein, H.; Scanlon, D. O. Spatial Electron-hole Separation in a One Dimensional Hybrid Organic-Inorganic Lead Iodide. *Sci. Rep.* **2016**, *6*, 20626.
(26) Veron, A. C.; Linden, A.; Leclaire, N. A.; Roedern, E.; Hu, S.; Ren, W.; Rentsch, D.; Nuesch, F. A. One-Dimensional Organic-Inorganic Hybrid Perovskite Incorporating Near-Infrared-Absorbing Cyanine Cations. *J. Phys. Chem. Lett.* **2018**, *9* (9), 2438−2442.
(27) Li, X.; Yang, J.; Song, Z.; Chen, R.; Ma, L.; Li, H.; Jia, J.; Meng, J.; Li, X.; Yi, M.; Sun, X. Naphthalene Diimide Ammonium Directed Single-Crystalline Perovskites with "Atypical" Ambipolar Charge Transport Signatures in Two-Dimensional Limit. *ACS Applied Energy Materials* **2018**, *1* (9), 4467−4472.
(28) Maheshwari, S.; Savenije, T. J.; Renaud, N.; Grozema, F. C. Computational Design of Two-Dimensional Perovskites with Functional Organic Cations. *J. Phys. Chem. C* **2018**, *122* (30), 17118−17122.
(29) Evans, H. A.; Lehner, A. J.; Labram, J. G.; Fabini, D. H.; Barreda, O.; Smock, S. R.; Wu, G.; Chabinyc, M. L.; Seshadri, R.; Wudl, F. (TTF)Pb 2 I 5: A Radical Cation-Stabilized Hybrid Lead Iodide with Synergistic Optoelectronic Signatures. *Chem. Mater.* **2016**, *28*, 3607−3611.
(30) Evans, H. A.; Labram, J. G.; Smock, S. R.; Wu, G.; Chabinyc, M. L.; Seshadri, R.; Wudl, F. Mono- and Mixed-Valence Tetrathiafulvalene Semiconductors (TTF)BiI4 and (TTF)4BiI6 with 1D and 0D Bismuth-Iodide Networks. *Inorg. Chem.* **2017**, *56*, 395.
(31) Maughan, A. E.; Kurzman, J. A.; Neilson, J. R. Hybrid Inorganic−Organic Materials with an Optoelectronically Active Aromatic Cation: (C 7 H 7) 2 SnI 6 and C 7 H 7 PbI 3. *Inorg. Chem.* **2015**, *54*, 370−378.
(32) Jiang, H.; Hu, P.; Ye, J.; Zhang, K. K.; Long, Y.; Hu, W.; Kloc, C. Tuning of the Degree of Charge Transfer and the Electronic Properties in Organic Binary Compounds by Crystal Engineering: A Perspective. *J. Mater. Chem. C* **2018**, *6*, 1884−1902.
(33) Zhang, J.; Xu, W.; Sheng, P.; Zhao, G.; Zhu, D. Organic Donor−Acceptor Complexes as Novel Organic Semiconductors. *Acc. Chem. Res.* **2017**, *50* (7), 1654−1662.
(34) Sun, L.; Zhu, W.; Yang, F.; Li, B.; Ren, X.; Zhang, X.; Hu, W. Molecular Cocrystals: Design, Charge-Transfer and Optoelectronic Functionality. *Phys. Chem. Chem. Phys.* **2018**, *20* (9), 6009−6023.
(35) Zhang, J.; Jin, J.; Xu, H.; Zhang, Q.; Huang, W. Recent Progress on Organic Donor−acceptor Complexes as Active Elements in Organic Field-Effect Transistors. *J. Mater. Chem. C* **2018**, *6* (14), 3485−3498.
(36) Zhu, L.; Yi, Y.; Fonari, A.; Corbin, N. S.; Coropceanu, V.; Bredas, J.-L.; et al. Electronic Properties of Mixed-Stark Organic Charge-Transfer Crystals. *J. Phys. Chem. C* **2014**, *118*, 14150−14156.
(37) Goetz, K. P.; Vermeulen, D.; Payne, M. E.; Kloc, C.; McNeil, L. E.; Jurchescu, O. D. Charge-transfer complexes: new perspectives on an old class of compounds. *J. Mater. Chem. C* **2014**, *2*, 3065−3076.
(38) Van Gompel, W. T. M.; Herckens, R.; Van Hecke, K.; Ruttens, B.; D'Haen, J.; Lutsen, L.; Vanderzande, D. Towards 2D layered hybrid perovskites with enhanced functionality: introducing charge-transfer complexes via self-assembly. *Chem. Commun.* **2019**, *55* (17), 2481−2484.
(39) Mitzi, D. B.; Medeiros, D. R.; Malenfant, P. R. L. Intercalated Organic-Inorganic Perovskites Stabilized by Fluoroaryl-Aryl Interactions. *Inorg. Chem.* **2002**, *41*, 2134−2145.
(40) Smith, M. D.; Pedesseau, L.; Kepenekian, M.; Smith, I. C.; Katan, C.; Even, J.; Karunadasa, H. I. Decreasing the electronic confinement in layered perovskites through intercalation. *Chemical Science* **2017**, *8*, 1960−1968.
(41) Dobrowolski, M. A.; Garbarino, G.; Mezouar, M.; Ciesielski, A.; Cyrański, M. K. Structural Diversities of Charge Transfer Organic Complexes. Focus on Benzenoid Hydrocarbons and 7,7,8,8-Tetracyanoquinodimethane. *CrystEngComm* **2014**, *16* (3), 415−429.
(42) Umari, P.; Mosconi, E.; De Angelis, F. Relativistic GW Calculations on CH3NH3PbI3 and CH3NH3SnI3 Perovskites for Solar Cell Applications. *Sci. Rep.* **2015**, *4*, 4467.
(43) Even, J.; Pedesseau, L.; Jancu, J.-M.; Katan, C. Importance of Spin-Orbit Coupling in Hybrid Organic/Inorganic Perovskites for Photovoltaic Applications. *J. Phys. Chem. Lett.* **2013**, *4*, 2999−3005.
(44) Giannozzi, P.; et al. Quantum Espresso: a modular and open-source software project for quantum simulations of materials. *J. Phys.: Condens. Matter* **2009**, *21*, 395502.
(45) Skùlason, E. Bader Analysis: Calculating the charge on individual atoms in molecules & crystals. Presentation in PDF.
(46) Warman, J. M.; De Haas, M. P.; Dicker, G.; Grozema, F. C.; Piris, J.; Debije, M. G. Charge Mobilities in Organic Semiconducting Materials Determined by Pulse-Radiolysis Time-Resolved Microwave Conductivity:Pi-Bond-Conjugated Polymers Versus Pi-Pi-Stacked Discotics. *Chem. Mater.* **2004**, *16*, 4600−4609.
(47) Gélvez-Rueda, M. C.; Hutter, E. M.; Cao, D. H.; Stoumpos, C. C.; Hupp, J. T.; Savenije, T. J.; Kanatzidis, M. G.; Grozema, F. C.; Renaud, N. Interconversion between Free Charges and Bound Excitons in 2D Hybrid Lead Halide Perovskites. *J. Phys. Chem. C* **2017**, *121* (47), 26566−26574.
(48) Savenije, T. J.; Ferguson, A. J.; Kopidakis, N.; Rumbles, G. Revealing the Dynamics of Charge Carriers in Polymer: Fullerene Blends Using Photoinduced Time-Resolved Microwave Conductivity. *J. Phys. Chem. C* **2013**, *117* (46), 24085−24103.
(49) Shi, D.; Adinolfi, V.; Comin, R.; Yuan, M.; Alarousu, E.; Buin, A.; Chen, Y.; Hoogland, S.; Rothenberger, A.; Katsiev, K.; et al. Low Trap-State Density and Long Carrier Diffusion in Organolead Trihalide Perovskite Single Crystals. *Science (Washington, DC, U. S.)* **2015**, *347* (6221), 519−522.
(50) Jackson, W. B.; Amer, N. M.; Boccara, A. C.; Fournier, D. Photothermal deflection spectroscopy and detections. *Appl. Opt.* **1981**, *20* (8), 1333−1344.
(51) Jensen, F. *Introduction to computational chemistry*; John Wiley & Sons, Inc.: 1999.
(52) *A Chemist's Guide to Density Functional Theory*, 2nd ed.; Koch, W., Holthausen, M. C., Eds.; Wiley-VCH: 2001.
(53) Yu, H. S.; et al. Perspective:Kohn-Sham density functional theory descending a staircase. *J. Chem. Phys.* **2016**, *145*, 130901.
(54) Hohenberg, P.; Kohn, W. Inhomogeneous Electron Gas. *Phys. Rev.* **1964**, *136*, B864−871.
(55) Kohn, W.; Sham, L. J. Self-Consistent Equations Including Exchange and Correlation Effects. *Phys. Rev.* **1965**, *140*, A1133−A1138.
(56) Grimme, S. Semiempirical GGA-type Density Functional Constructed with a Long-Range Dispersion Correction. *J. Comput. Chem.* **2006**, *27*, 1787−1799.
(57) Perdew, J. P.; Burke, K.; Ernzerhof, M. Generalized Gradient Approximation Made Simple. *Phys. Rev. Lett.* **1996**, *77* (18), 3865−3868.
(58) Dovesi, R.; Orlando, R.; Erba, A.; Zicovich-Wilson, C. M.; Civalleri, B.; Maschio, L.; Ferrabone, M.; De La Pierre, M.; D'Arco, P.; Noel, Y.; Causa, M.; Rerat, M.; Kirtman, B.; Casassa, S. CRYSTAL14: A program for the *ab initio* investigation of crystalline solids. *Int. J. Quantum Chem.* **2014**, *114*, 1287.
(59) Dovesi, R.; Saunder, V. R.; Roetti, C.; Orlando, R.; Zicovich-Wilson, C. M.; Pascale, F.; Civalleri, B.; Doll, K.; Harrison, N. M.; Bush, I. J.; D'Arco, P.; Llunell, M.; Causà, M.; Noël, Y. *CRYSTAL14 User's Manual*; University of Torino: Torino, 2014.
(60) Dovesi, R.; Erba, A.; Orlando, R.; Zicovich-Wilson, C. M.; Civalleri, B.; Maschio, L.; Rerat, M.; Casassa, S.; Baima, J.; Salustro, S.; Kirtman, B. Quantum-mechanical condensed matter simulations with CRYSTAL. *WIREs Comput. Mol. Sci.* **2018**, *8*, No. e1360.

DOI: 10.1021/acs.chemmater.9b01289
Chem. Mater. 2019, 31, 6880−6888

(61) Dovesi, R.; Saunder, V. R.; Roetti, C., Orlando, R.; Zicovich-Wilson, C. M.; Pascale, F.; Civalleri, B.; Doll, K.; Harrison, N. M. *CRYSTAL17 User's Manual*; University of Torino: Torino, 2017.

DOI: 10.1021/acs.chemmater.9b01289
Chem. Mater. 2019, 31, 6880−6888